

RESEARCH ARTICLE | JANUARY 02 2025

Dimensional confinement and superdiffusive rotational motion of uniaxial colloids in the presence of cylindrical obstacles

Vikki Anand Varma  ; Sujin B. Babu  



J. Chem. Phys. 162, 014901 (2025)

<https://doi.org/10.1063/5.0238648>



View
Online



Export
Citation

Articles You May Be Interested In

Mobile obstacles accelerate and inhibit the bundle formation in two-patch colloidal particle

J. Chem. Phys. (August 2019)

Active motion of tangentially driven polymers in periodic array of obstacles

J. Chem. Phys. (December 2023)

Dimensional confinement and superdiffusive rotational motion of uniaxial colloids in the presence of cylindrical obstacles

Cite as: J. Chem. Phys. 162, 014901 (2025); doi: 10.1063/5.0238648

Submitted: 13 September 2024 • Accepted: 17 December 2024 •

Published Online: 2 January 2025



View Online



Export Citation



CrossMark

Vikki Anand Varma and Sujin B. Babu ^{a)}

AFFILIATIONS

Out of Equilibrium Group, Department of Physics, Indian Institute of Technology Delhi, New Delhi 110016, India

^{a)}Author to whom correspondence should be addressed: sujin@physics.iitd.ac.in

ABSTRACT

In biological systems such as cells, the macromolecules, which are anisotropic particles, diffuse in a crowded medium. In the present work, we have studied the diffusion of spheroidal particles diffusing between cylindrical obstacles by varying the density of the obstacles as well as the spheroidal particles. Analytical calculation of the free energy showed that the orientational vector of a single oblate particle will be aligned perpendicular, and a prolate particle will be aligned parallel to the symmetry axis of the cylindrical obstacles in equilibrium. The nematic transition of the system with and without obstacles remained the same, but in the case of obstacles, the nematic vector of the spheroid system always remained parallel to the cylindrical axis. The component of the translational diffusion coefficient of the spheroidal particle perpendicular to the axis of the cylinder is calculated for the isotropic system, which agrees with analytical calculation. When the cylinders overlap such that the spheroidal particles can only diffuse along the direction parallel to the axis of the cylinder, we can observe dimensional confinement. This was observed by the discontinuous fall of the diffusion coefficient, when plotted against the chemical potential both for a single particle and for a finite volume fraction. The rotational diffusion coefficient quickly reached the bulk value as the distance between the obstacles increased in the isotropic phase. In the nematic phase, the rotational motion of the spheroid should be arrested. We observed that even though the entire system remained in the nematic phase, the oblate particle close to the cylinder underwent a flipping motion. The consequence is that when the rotational mean squared displacement was calculated, it showed a super-diffusive behavior even though the orientational self-correlation function never relaxed to zero, showing this to be a very local effect.

Published under an exclusive license by AIP Publishing. <https://doi.org/10.1063/5.0238648>

I. INTRODUCTION

The role of shape anisotropy on the diffusivity of the colloids has been studied extensively. Most of these studies are performed for the bulk system, assuming that particles are suspended in a medium. However, in natural systems,^{1,2} the diffusivity and other dynamical behaviors change due to many factors such as obstacles, finite size of the suspended particles, and confinement.^{3–5} It is also known that the diffusivity decreases due to the crowding effect caused by the slowly moving heavy particles⁶ and also polydispersity leads to an anomalous diffusion behavior.⁷ In some cases, ions have been shown diffusing opposite to the applied potential due to bonding with the heavy molecules.^{8,9} In the presence of the activity, the diffusivity of the isotropic particles has been shown to enhanced.^{10–12}

Local diffusivity has been found to vary with the change in the width of the channel or the radius of the obstacle.^{13,14} In addition, effective diffusivity has been found to reduce with the increase in the obstacle density.^{15,16} Diffusivity has been shown to be affected by the presence of the effective force field, e.g., gravity.¹⁷ In the passive particle system, diffusivity has been shown to decrease with the increase in obstacle concentration,¹⁸ and the nature of glass transition at high densities has also been studied.¹⁹ In the 2D system, the presence of obstacles leads to a sub-diffusive behavior^{20,21} for the Brownian particle. The 2D confinement also leads to the anomalous behavior, in the presence of obstacles.²² The confinement and the presence of obstacles lead to phase rich behaviors by changing the structural properties. In the presence of solute–solvent attractive interaction, colloids have been observed altering the alignment of the

nematic fluid.²³ The liquid crystals have been found aligning with the surface of the large spheres sandwiched between the two parallel surfaces,²⁴ forming a Saturn ring kind of structure. The study of such systems also opens a pathway for the application in various engineering solutions, e.g., electronics.

These observed effects depend upon the type of confinement,²⁵ absorption properties of the confining walls,²⁶ the surface roughness of the wall,²⁷ and drift forces.²⁸ Apart from these physical and chemical properties of fluid and confining geometry, the dynamics of colloidal particles also depend upon their shape,²⁹ especially in the active particle system.³⁰ For a 2D system, having confinement along one axis, the system has been shown to follow the behavior of a 1D system.³ In these systems, anisotropic particles can behave differently than the isotropic particle system. In the presence of anisotropic particles, the role of obstacles has been paid less attention, specifically the study of the dynamics and structure while considering the interaction of the phase-rich anisotropic particles with obstacles.

These systems have been studied extensively by using both analytical and experimental approaches. For example, the mean first passage time³¹ is shown to be an important parameter governing the kinetics of the system, especially for diffusion-limited cluster aggregation (DLCA) processes. As another example, the diffusivity of the polymer has been studied using blob theory,³² an approximation done in terms of average particle size. In the presence of periodic obstacles, analytical relations have been derived for the diffusion coefficient considering them as point particles.^{33,34} The effective diffusivity in the dimensional confinement for the two-dimensional system has been shown for the point particles,³⁵ where an obstacle configuration leads the particles to move within a channel. Few lattice-based models are also proposed for the study of the diffusion of particles with obstacles.³⁶ In most of the studies performed previously on a similar kind of system, the radius of the obstacles considered is much bigger than the size of the Brownian particles.³⁷ In all these studies, the shape anisotropy of the particles was not considered. In a case, where analytical approaches become very difficult to follow, simulation can be a useful tool. In simulation, different coarse-grained models provide an excellent advantage for studying comparatively complex systems. The anomalous diffusivity in the presence of crowded media has been studied in periodic obstacles where the motion becomes diffusive in the long time limit.^{6,38}

In the present work, we have considered a system of anisotropic particles in the presence of the periodic arrangement of cylindrical obstacles. Depending upon the density of the obstacles, the system is effectively confined. For example, at the high density of cylindrical obstacles,²⁸ particles are constrained to diffuse in one dimension. In this way, at different obstacle configurations, we studied the structure, kinetics, and dynamics emerging in such a phase rich system of hardcore particles.

For highly elongated particles, the system is well known to encounter nematic alignment. In our case, the director axis has been found to align with the obstacles. In the present study, we also observed that the rotational dynamics of the oblate particles are not freezing despite being in the nematic phase. Nematic-isotropic transition lines have been found to shift in the two-component system.³⁹ In the presence of confinement, the orientation of the nematic director could be controlled as well, for example hard rods have been found to align along the plane of the substrate, shown using

density functional theory.⁴⁰ Alignment of the particles depending upon the boundary of the medium has been found to govern the crack patterns,^{41,42} growth of bacteria,⁴³ etc. The presence of obstacles has also been found to affect the self-assembly of Brownian particles.^{44–46} The presence of different types of particles or obstacles also alters the phase boundary, as shown in the binary mixture of hard-spheroid–sphere and sphere–rod systems.^{47,48} However, in the presence of cylindrical obstacles, despite governing the orientation of the nematic director, the system shows no alteration in its nematic–isotropic phase boundary. These kinds of behaviors can help us design colloidal systems with robust control⁴⁹ over structural properties for a variety of applications.

II. SIMULATION METHOD

We start the simulation by randomly distributing N number of particles in a cubic box with edge length L , where all the lengths have been considered in the unit of $d = 1$, the diameter of the spherical Brownian particle. Thus, the volume fraction of the particles is defined over the available volume $V - \pi r_o^2 L$ such that $\phi = \frac{N}{V - \pi r_o^2 L}$, where $V = L^3$. The volume of the anisotropic particle with the major axis length a and minor axis length b having aspect ratio $p = a/b$ is always kept equal to the volume of a sphere with diameter $d = 1$. Thus, the volume fraction of the spheroidal particles is given by $\pi/6ab^2$. The shape anisotropic spheroidal particle orientation vector \hat{n} has been considered along its symmetry axis. The number of particles considered is in the range of 500–2500, and p is simulated in the range 0.25–4. The cylindrical obstacles of radius r_o and length L are placed parallel to each other along the z direction on a square lattice. A periodic boundary condition is applied in the cubic box. The density of the obstacles is defined in terms of the area fraction ϕ_o calculated in the plane perpendicular to the axis of cylinders, where $\phi_o = \rho_o \pi r_o^2$ such that ρ_o is the number fraction of the obstacles defined as $\rho_o = \frac{N_o}{L^2}$.

We used the ellipsoid contact function (ECF)⁵⁰ to check the overlap between the spheroids. The same criterion is used to check the overlap between a cylinder and a particle. A cylinder is created by positioning spheres close enough to each other along the cylindrical axis so that the surface remains featureless.

To perform the dynamics of the particles, we used the Brownian-cluster-dynamics (BCD) simulation technique.⁵¹ Using this method structure, kinetics and dynamics for a variety of different types of Brownian particles such as sphere^{52–54} and spheroids^{55,56} are studied. In this method, we randomly select particles $2N$ times and perform either a rotational or a translational movement with equal probability. It ensures that each particle is translated or rotated at least once, in each simulation step. For the translational movement, we displace the particle in a random direction with a fixed step length S_T . Similarly, for the rotational motion, the tip of the orientation vector \hat{n} performs a 2d random walk over the surface of a sphere, with a fixed rotational step length S_R , such that S_T and S_R satisfy the following relation:

$$S_R^2 = 2S_T^2. \quad (1)$$

The relation between the simulation time t_{Sim} and the physical time t_{Phy} is given by $\frac{t_{Phy}}{t_0} = t_{Sim} \frac{S_T^2}{d^2}$,³⁹ where t_0 is the time required for a

single sphere to diffuse through a distance of its own diameter. After performing each movement step, we check the overlap condition of the hardcore particle and if the particles are overlapping, then we reject that particular movement.³⁹

A. Dynamics of the shape anisotropic particles

To implement the dynamics for the shape anisotropic particles, we calculate the translational displacement S_T along a direction parallel (s_T^{\parallel}) and perpendicular (s_T^{\perp}) to the spheroid's symmetry axis \hat{n} .³⁹ S_T^{\parallel} is given by

$$\frac{S_T^{\perp,\parallel}}{S_T} = \sqrt{\frac{d}{2bG_T^{\perp or \parallel}}}, \quad (2a)$$

$$\frac{S_R^e}{S_T} = \sqrt{\frac{2}{G_\theta}}, \quad (2b)$$

where $G_T^{\perp or \parallel}$ is Perrin's friction factor for the diffusion of the particle perpendicular and parallel to \hat{n} and G_θ is the friction factor for the rotational motion, which is calculated analytically for the stick boundary condition: for the prolate ($p > 1$) case,

$$G_T^{\parallel} = \frac{4}{3} \left[\frac{p}{(1-p^2)} + \frac{2p^2-1}{(p^2-1)^{3/2}} \ln \left(p + \sqrt{p^2-1} \right) \right]^{-1}, \quad (3a)$$

$$G_T^{\perp} = \frac{8}{3} \left[\frac{p}{(p^2-1)} + \frac{2p^2-3}{(p^2-1)^{3/2}} \ln \left(p + \sqrt{p^2-1} \right) \right]^{-1}, \quad (3b)$$

$$G_\theta = \frac{2}{3} \frac{(p^4-1)}{p} \left[\frac{(2p^2-1)}{\sqrt{p^2-1}} \ln \left(p + \sqrt{p^2-1} \right) - p \right]^{-1}, \quad (3c)$$

and for the oblate ($p < 1$) case, we have

$$G_T^{\parallel} = \frac{4}{3} \left[\frac{p}{(1-p^2)} + \frac{1-2p^2}{(1-p^2)^{3/2}} \arccos(p) \right]^{-1}, \quad (4a)$$

$$G_T^{\perp} = \frac{8}{3} \left[\frac{p}{(p^2-1)} + \frac{3-2p^2}{(1-p^2)^{3/2}} \arccos(p) \right]^{-1}, \quad (4b)$$

$$G_\theta = \frac{2}{3} \frac{(p^4-1)}{p} \left[\frac{(2p^2-1)}{\sqrt{1-p^2}} \arccos(p) - p \right]^{-1}. \quad (4c)$$

The parameter G is 1, and $p = 1$ means that the particle is spherical.

B. Surface energy calculation close to the obstacle-particle interface

The grand thermodynamical potential Ω can be expressed as a functional of density ρ ,^{40,57}

$$\Omega\{\rho(\mathbf{r}, \omega)\} = F_{id} + F_f + F_V + F_\mu, \quad (5)$$

where F_{id} is the ideal gas contribution given by

$$F_{id} = \int [\ln \Lambda^3 \rho(\mathbf{r}, \omega) - 1] \rho(\mathbf{r}, \omega) d\omega d\mathbf{r}. \quad (6)$$

The inter-particle interaction is counted in terms of F_f given by

$$F_f = \int f_2(\mathbf{r}_1, \mathbf{r}_2, \omega_1, \omega_2) \rho(\mathbf{r}_1, \omega_1) \rho(\mathbf{r}_2, \omega_2) d\omega_1 d\omega_2 d\mathbf{r}_1 d\mathbf{r}_2, \quad (7)$$

where $f_2(\mathbf{r}_1, \mathbf{r}_2, \omega_1, \omega_2)$ is the Mayer function. This function has a value 1 for overlapping and 0 for non-overlapping conditions. F_μ corresponds to the bulk chemical potential, given by

$$F_\mu = -\beta \mu \int \rho(\mathbf{r}, \omega) d\omega d\mathbf{r}, \quad (8)$$

where μ is the chemical potential of the system at a particular volume fraction in the absence of obstacles. F_V is the free energy contribution in the presence of a cylinder given by

$$F_V = \int V_o(\mathbf{r}, \omega) \rho(\mathbf{r}, \omega) d\omega d\mathbf{r}. \quad (9)$$

We express \mathbf{r} in cylindrical coordinates as $\mathbf{r} = \varrho \hat{\phi} + z \hat{z}$. In Cartesian coordinates, it can be written as $\mathbf{r} = \varrho \cos(\theta) \hat{i} + \varrho \sin(\theta) \hat{j} + z \hat{k}$.

We express the potential in the presence of cylindrical obstacles as follows:

$$V_o = \begin{cases} +\infty, & \varrho < \varrho_m(\theta, \omega, r_o), \\ 0, & \varrho > \varrho_m(\theta, \omega, r_o), \end{cases} \quad (10)$$

where r_o is the radius of the cylindrical obstacles and ϱ_m is the minimum distance between the center of the obstacle and the center of mass of the Brownian particle, which depends upon the relative orientation of the particle and the cylinder body. For a particular system, since we have r_o as constant, V_o can be expressed as follows:

$$V_o = \begin{cases} +\infty, & \varrho < \varrho_m(\theta, \omega), \\ 0, & \varrho > \varrho_m(\theta, \omega). \end{cases} \quad (11)$$

We minimize $\Omega\{\rho(\mathbf{r}, \omega)\}$ with respect to $\rho(\mathbf{r}, \omega)$, which leads to

$$\rho(\mathbf{r}, \omega) = \rho_b(\mathbf{r}, \omega) \exp[-V_o(\varrho, \theta, \omega)], \quad (12)$$

where $\rho_b(\mathbf{r}, \omega)$ is the bulk properties of the Brownian particles that can be retrieved when V_o is zero,

$$\rho_b(\mathbf{r}, \omega) = \frac{1}{\Lambda} e^{\beta \mu} \times \exp \left[\int f_2(\mathbf{r}, \mathbf{r}', \omega', \omega) \rho(\mathbf{r}, \omega) \rho(\mathbf{r}', \omega') d\mathbf{r}' d\omega' \right]. \quad (13)$$

The term that represents the bulk property can also be written as $\rho_b(\mathbf{r}, \omega) = \rho_b f(\omega)$ ⁵⁷ assuming a uniform distribution of the particles, where $f(\omega) = f(\mathbf{n}_1 \cdot \hat{n})$ is the angular distribution of the particles calculated from the director of the nematic-alignment \mathbf{n}_1 . $f(\omega)$ can

be normalized with 4π in the case of isotropic phase. To calculate the system's energy close to the obstacles, we consider the symmetry of the cylindrical obstacle along \hat{z} . Now, ρ can be expressed as $\rho(\varrho, \theta, \omega)$, which is given by

$$\rho(\varrho, \theta, \omega) = \rho_b f(\omega) \exp[-V_o(\varrho, \theta, \omega)]. \quad (14)$$

To calculate the surface energy per unit length along the symmetry axis of the obstacle, we take both the densities, bulk and close to the surface, and subtract the energy calculated by using Eqs. (6)–(9) and (12). The surface energy per unit length, ψ_l , is given by

$$\frac{\psi_l}{k_B T} = -\frac{S}{k_B} - \frac{\Delta\mu}{k_B T} \xi, \quad (15)$$

$$\Delta\mu = \mu - k_B T \ln(\Lambda^3 \rho_b / 4\pi), \quad (16)$$

$$\begin{aligned} \xi &= \int_{\theta=0}^{2\pi} \int_{\omega=0}^{\pi} \int_{\varrho=r_o}^{\infty} [\rho(\varrho, \theta, \omega) - \rho_b f(\omega)] d\varrho d\theta d\omega \\ &= -\frac{1}{2} \rho_b \int_{\theta=0}^{2\pi} \langle (\rho_m^2(\omega, \theta) - r_o^2) \rangle_{f(\omega)} d\theta. \end{aligned} \quad (17)$$

The other term contributing to the surface energy per unit length contains the rotational term coming from the anisotropic configuration of the particle and is given by

$$S_{rot} = \frac{1}{2} \rho_b \int_{\theta=0}^{2\pi} \langle (\rho_m^2(\omega, \theta) - r_o^2) \ln[4\pi f(\omega)] \rangle_{f(\omega)} d\theta, \quad (18)$$

where S is given by

$$S = S_{rot} + S_{tr}, \quad (19)$$

such that $S_{tr} = S_{tr}^{id} + S_{tr}^m$, where the ideal and inter-molecular terms can be defined as

$$S_{tr}^{id} = -\frac{1}{2} \rho_b \int_{\theta=0}^{2\pi} \langle (\rho_m^2(\omega, \theta) - r_o^2) \rangle_{f(\omega)} d\theta, \quad (20)$$

$$\begin{aligned} S_{tr}^m &= -\frac{1}{2} \left[\int f_2(\varrho, \omega, \mathbf{r}', \omega') \rho(\varrho, \omega) \rho(\mathbf{r}', \omega') d\mathbf{r}' d\omega' d\varrho d\omega \right. \\ &\quad \left. - \rho_b^2 \int f_2(\varrho, \omega, \mathbf{r}', \omega') f(\omega) f(\omega') d\mathbf{r}' d\omega' d\varrho d\omega \right]. \end{aligned} \quad (21)$$

The average surface energy per unit area at the obstacle bulk interface can be expressed as

$$\frac{\Gamma}{k_B T} = \frac{3a}{2\pi[(3a/2 + r_o)^2 - r_o^2]} \frac{\psi_l}{k_B T}. \quad (22)$$

Here, the greater value of μ contributes to the alignment of the particles along the cylinder's axis. In other words, for a higher ϕ region, where μ is greater, the parallel alignment is ensured. We took a value of μ close to the isotropic–nematic interface and calculated Eqs. (16)–(18), (20), and (21), where Eq. (21) was calculated by using the Monte Carlo and curve-fitting methods, as the

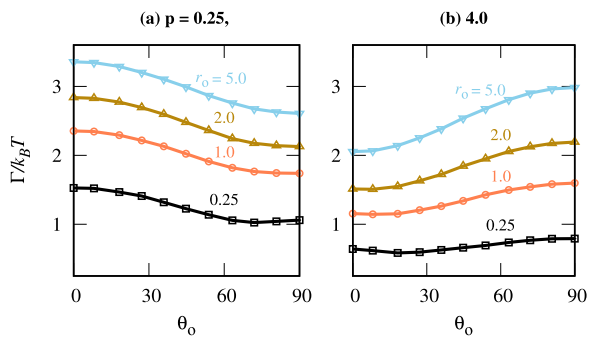


FIG. 1. Surface energy is calculated at different θ° , for both the oblate ($p = 0.25$) and prolate ($p = 4.0$) systems. Shown for the different radii of the cylindrical obstacles, as depicted in the plots. The oblate and prolate systems are energetically favored at $\theta^\circ = 90$ and 0 , respectively.

function is smooth all over the region of integral. Figure 1 shows the variation in $\Gamma/k_B T$ with the angle between the orientation of the director and the axis of the cylinder, θ_o . For the oblate case ($p = 0.25$), the angle perpendicular to the cylinder's axis is favored, over the parallel arrangement. In the case of prolate ($p = 4.0$), we have a parallel alignment favored over the perpendicular alignment. The energy difference between the parallel and perpendicular alignments reduces as the radius of the obstacle r_o decreases. For thin cylinders, the energy minima occur slightly away from $\theta_o = 90^\circ$ in the oblate and 0° in the prolate case. As we increase r_o , the difference between $\Gamma/k_B T$ of minimum and maximum energy configurations increases. In other words, the control of the nematic axis is enhanced with the increase in the radius of the cylinder⁵⁸ at a constant number density of the obstacles.

III. RESULTS

A. Kinetics of the evolution of nematic-alignment in the presence of cylindrical obstacles

Figure 1 shows the surface energy per unit volume close to the cylinder–bulk interface as given by Eq. (22), where we considered only the hardcore repulsion interaction between the cylinder and ellipsoid and between ellipsoid and ellipsoid. In addition, we have considered only a single cylindrical obstacle. In Fig. 1(a), we observe that the surface energy is minimum when the symmetry axis of the oblate particle ($p = 0.25$) is perpendicular to the cylindrical axis. For the prolate particle ($p = 4.0$), we observe that minimum surface energy configuration happens when the symmetry axis of the particle is parallel to the cylindrical axis. Thus, it seems that the presence of an obstacle will assist in the nematic transition for anisotropic particles.

We did not observe any significant effect on the nematic–isotropic phase line for the system where the distance between the obstacles is large enough for the particles to rotate freely. However, in the presence of obstacles at high densities, a large fraction of spheroids close to the wall remain aligned along the wall in comparison with the small fraction of particles present in the bulk isotropic regions, contributing to the high nematic order-parameter value. In all such cases, where the distance between the obstacles becomes comparable to the size of the particles, S

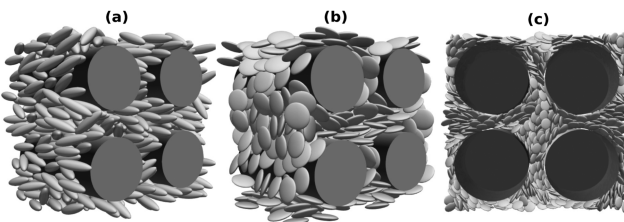


FIG. 2. Snapshot of the system in nematic-phase, shown at $\phi = 0.45$ for (a) $p = 4.0$, $r_o = 2.0$, and $\phi_o = 0.4$; (b) $p = 0.25$, $r_o = 2.0$, and $\phi_o = 0.4$; and (c) $p = 0.25$, $r_o = 5.0$, and $\phi_o = 0.55$, where all the three systems are in nematic phase.

remains high (e.g., $S = 0.65$ for $p = 4$, $\phi = 0.38$ at $\phi_o = 0.5$), which agrees with the previous observations.⁵⁹

We initiate the system by putting the spheroids in an energetically less favorable state as obtained from the obstacle–bulk surface energy calculation (see Fig. 1). For the oblate particle, nematic director is less favored along the symmetry axis of the cylinders, and for the prolate case, it is less favored along the perpendicular plane of the symmetry axis of the obstacles. Thus, the ellipsoids in the initial configuration are already in the nematic phase. Relaxation of the angle between the symmetry axis of the ellipsoid and the cylindrical axis for $\phi = 0.5$, $\rho_o = 0.005$, and $r_o = 2.0$ can be observed in Fig. 3(a). It seems that the rotational kinetics of the symmetry axis of the ellipsoids relaxes slowly up to a time of 200, and then, suddenly all the ellipsoids rearrange to the minimum surface energy configuration [see Figs. 2(a) and 2(b)] obtained from a single ellipsoidal calculation. Also note that in the absence of obstacles at $\phi = 0.5$, the equilibrium configuration of the ellipsoids is a nematic phase. Figure 3(b) shows the evolution of the nematic phase order parameter S , which is the largest eigenvalue of the tensor Q , defined by

$$Q_{\alpha\beta} = \frac{3}{2} \frac{1}{N} \sum_i \langle (n_\alpha)_i (n_\beta)_i \rangle - \frac{1}{2} \delta_{\alpha\beta}, \quad (23)$$

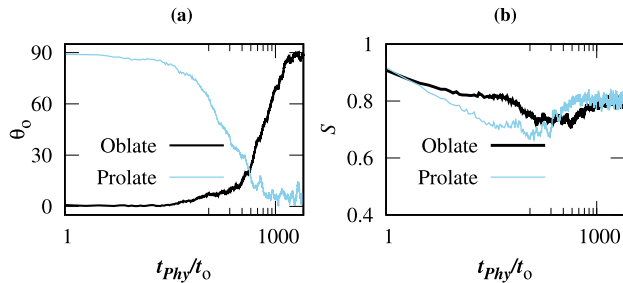


FIG. 3. (a) Evolution of the director of oblate and prolate systems is shown for $r_o = 2.0$ and a low $\phi_o = 0.063$, at $\phi = 0.5$. The system starts initially from an unfavorable condition for prolate ($p = 4.0$) at $\theta_o = 90^\circ$ and oblate ($p = 0.25$) at $\theta_o = 0^\circ$, where θ_o is the angle between the nematic director and the axis of the cylindrical obstacles. (b) The evolution of the order parameter is shown for both the oblate and prolate systems. Both the systems show stability after a long time limit ($t_{phys} > 1000$).

where n_α and n_β are the components of the particle's orientation vector (\hat{n}) with $\alpha, \beta \in x, y, z$.

As the system moves toward the equilibrium state, the S parameter falls at initial times but remains well above the value 0.3, showing that the system never passes through the isotropic phase. In other words, the system remains in the nematic phase throughout the evolution in both prolate and oblate cases. The fall in the S parameter indicates the gradual change in the orientation of the particles, which is initiated from the cylinder–bulk interface and expands toward the bulk region of the ellipsoidal particles. This shows that we can make an ellipsoid particle system undergo a transition from an unfavorable nematic phase to a favorable nematic phase due to the presence of the cylindrical obstacle.

Figure 4 shows the kinetics of the evolution of θ_o for both oblate and prolate cases in the presence of obstacles. In the case of constant $\rho_o = 0.005$, the kinetics of the system is higher for the system with cylinders having a greater radius, as shown in Figs. 4(a) and 4(b). A system with $r_o = 5$ evolves faster than a system with $r_o = 2$. It can be explained by considering the effect of $\phi_o = \rho_o \pi r_o^2$ such that ϕ_o increases with the increase in r_o . A system with a higher

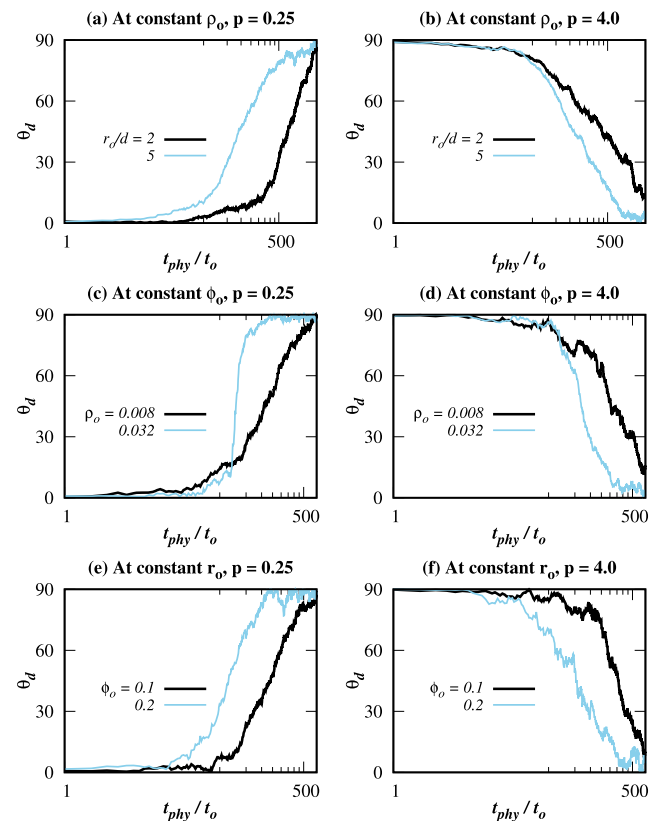


FIG. 4. Evolution of the directors shown at a different configuration for both the oblate and prolate systems. (a) Prolate and (b) oblate are shown at $\phi = 0.5$ for different r_o/d , at constant $\rho_o = 0.005$. (c) and (d) Evolution of the oblate and prolate systems for different ρ_o and at constant $\phi_o = 0.1$. (d) and (f) System's evolution for different ϕ_o , at constant $r_o = 2.0$.

surface of the obstacles will have a higher total surface energy difference between favorable and unfavorable states, which results in a faster evolution toward the favorable state. Apart from that, $\Delta\Gamma_m$ has a higher value for the obstacles having a greater r_o ; this effect is not as dominating as the effect of obstacles–bulk interface interaction. In Figs. 4(c) and 4(d), where both the systems were simulated at constant $\phi_o = 0.1$, it has been shown that the system with higher $\rho_o = 0.032$ shows a faster evolution to the favorable state.

At constant ϕ_o , reducing the radius of the cylinders will increase the surface area as the number of cylinders increases in the system. In other words, the sky-blue line representing a system with $r_o = 1.0$ has a surface area of the obstacles two times greater than the system with $r_o = 2.0$, at constant ϕ_o . Therefore, despite having $\Delta\Gamma_m$ higher, the system with $r_o = 2$ shows a slower evolution than the system with $r_o = 1$. Similar observations are shown in Figs. 4(e) and 4(f) for the oblate and prolate systems, respectively. For the same r_o , the system with higher ϕ_o has a greater surface area in contact with the ellipsoids, and therefore, the system with higher ϕ_o evolves faster.

To show the structural properties of the nematic phase, we calculated the radial distribution function $g(r)$, as shown in Fig. 5. For $r_o = 5$ and $\rho_o = 0.005$, we have the $g(r)$ curve deviating from the usual $g(r) = 1$ (solid line), due to the absence of particles in the obstacle regions, for both oblate and prolate cases, which is shown in Figs. 5(a) and 5(b), respectively. The dotted line represents the system with spherical particles simulated at the same configuration. However, the peaks of the curves are similar to the bulk system, where again the deviation represents a large inaccessible region for the diffusing particles. The black lines represent the system with

$r_o = 2$ simulated at the same $\rho_o = 0.005$, which show characteristics similar to the bulk phase, where we have a small inaccessible region in comparison with $r_o = 5$. For both systems, the local structure remains similar to the bulk phase. Figures 5(c) and 5(d) represent the system of oblate and prolate particles, respectively, simulated at constant $\phi_o = 0.1$ for different obstacle radii, where the sky-blue lines represent $r_o = 1$ and the black lines represent $r_o = 2$. The system, again, can be observed to be similar to the bulk phase. Figures 5(e) and 5(f) show $g(r)$ for the system of oblate and prolate particles, respectively, simulated at constant $r_o = 2$ for different obstacle densities, where the sky-blue lines represent $\phi_o = 0.2$ and the black lines represent $\phi_o = 0.1$.

To understand the alignment of the particles in the nematic phase, we have shown $g(\theta)$ as a function of the angle θ , where $g(\theta)$ is the distribution of the angle θ , formed between \hat{n} of any two particles. For a perfectly aligned nematic system, it will show sharp peaks at $\theta = 0^\circ$ and 180° . Figures 6(a) and 6(b) show the distribution $g(\theta)$ for prolate and oblate particles, respectively, at constant $\rho_o = 0.005$ at two different obstacle radii $r_o = 2$ and $r_o = 5$.

In the oblate case, the particles' orientation remains perpendicular to the direction of cylindrical axis, causing misalignment, which can be observed in the $G(\theta)$ distribution [Fig. 6(a)]. It has an effect on the dynamics of the system, where it shows an anomalous rotational behavior, which has been discussed in Sec. III B. Prolate particles align with its orientation parallel to the direction of the cylindrical axis, which enhances the particles' alignment [Fig. 6(b)]. Figures 6(c) and 6(d) show the alignment calculated for the same ϕ_o , where we observe that increasing the number density while decreasing the radius of the cylinders leads to better alignment in the case

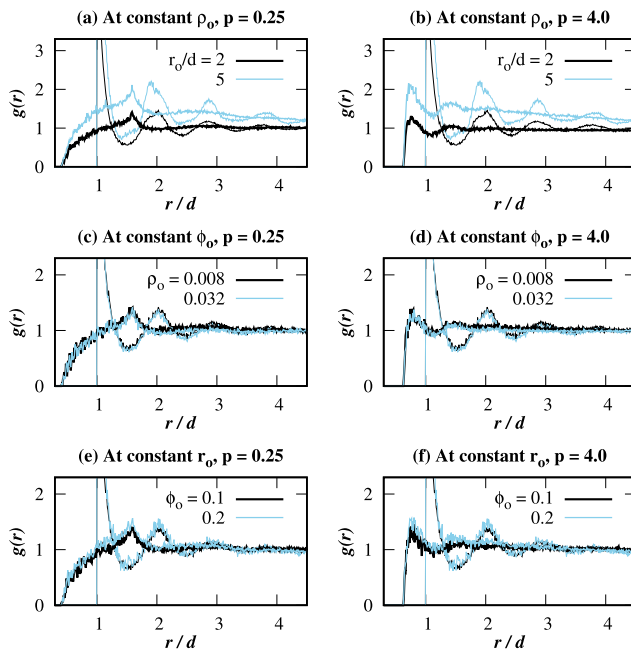


FIG. 5. $g(r)$ is shown for the system in the nematic phase for both prolate and oblate particles: (a) and (b) at constant $\rho_o = 0.005$, (c) and (d) at constant $\phi_o = 0.1$, and (e) and (f) at constant $r_o = 2.0$. The thin lines represent the system of spheres equilibrated at the same configuration.

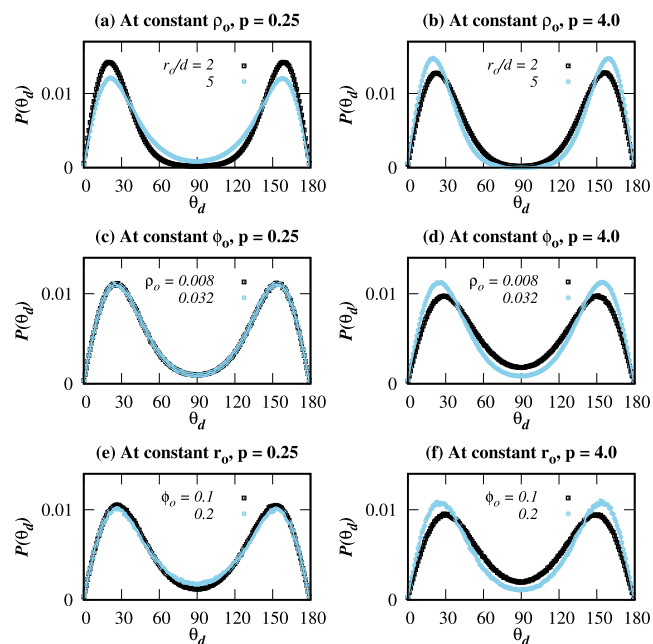


FIG. 6. $g(\theta)$ is shown for the system in the nematic phase for both prolate and oblate particles: (a) and (b) at constant $\rho_o = 0.005$, (c) and (d) at constant $\phi_o = 0.1$, and (e) and (f) at constant $r_o = 2.0$.

of prolate particles, while for the case of oblate particles, it remains nearly the same. With increasing ϕ_o , we observed a small decrease in alignment for the oblate particles [see Fig. 6(e)], whereas prolate shows better alignment [see Fig. 6(f)]. In all three cases, the behavior of oblate has been seen to be opposite to the prolate case.

B. Dynamics of the system in the presence of obstacles

The translational diffusion dynamics of a tracer spherical particle in crowded media depends only upon the accessible volume.⁶⁰ The accessible volume is defined as the volume accessible to the center of mass of a tracer particle. That means as we increase the volume fraction, the diffusivity decreases and becomes dependent upon the packing fraction.^{39,61} Here, we are exploring the dynamics of the ellipsoidal particle far away from the nematic transition. We also did not take into account the hydrodynamic effect. When we assume that the fluid particles are very small in size compared to the size of the obstacles, the effect of hydrodynamics on the system remains minimal.^{62,63} We have also considered the surface of the obstacles to be smooth and featureless.²⁸

The two-dimensional diffusivity of the diffusing point particles has been calculated analytically, in the presence of periodically arranged immobile disks.³⁷ In order to compare with the analytical results for finite size and shape of the diffusing particles, we considered the obstacle configuration in terms of the trap size given as q having a trap opening width of w , as shown in Fig. 7(b).⁶⁴ Here, q and w can be expressed in terms of obstacle radius (r_o) and lattice density (ρ_o),

$$w = \sqrt{\frac{1}{\rho_o}} - 2r_o, \quad (24a)$$

$$q = \sqrt{\frac{2}{\rho_o}} - 2r_o. \quad (24b)$$

The effective translational diffusivity of the point particles in the presence of the 2d array of the obstacles is given by⁸

$$D_T^{eff} = \frac{1}{\langle w'(x) \rangle \langle 1/w'(x) D(x) \rangle}, \quad (25)$$

where $w(x)$ is the channel's width, which changes with positions. $w'(x)$ is the derivative of the channel width with respect to position.³⁷ $D(x)$ is the position dependent diffusivity.

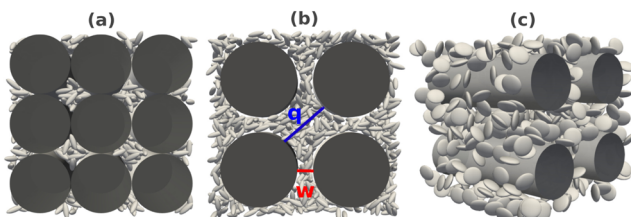


FIG. 7. Snapshot of the isotropic system shown at particle concentration $\phi = 0.2$ for different obstacle configurations: (a) $q = 3.0$, $w = 0.0$, and $r_o = 3.6$; (b) $q = 7.0$, $w = 2.0$, and $r_o = 5.0$; and (c) $q = 2.3$, $w = 2.0$, and $r_o = 2$, where w and q are the lengths measured in units of d_o , as shown in panel (b).

We consider the diffusion coefficient to be a constant (independent of the position) and equal to D_2^P (maximum possible diffusivity for a given obstacles' lattice configuration) and solve Eq. (25). The analytical expression for the effective diffusivity due to Fick–Jacob D_T^{FJ} is then given by³⁷

$$\frac{D_T^{FJ}}{D_2^P} = \frac{1}{(1 - \frac{\pi}{4} f_w^2)} \left(\frac{2}{\sqrt{1 - f_w^2}} - \arctan \left(\frac{\sqrt{1 + f_w}}{1 - f_w} \right) - \frac{\pi}{2} + 1 - f_w \right). \quad (26)$$

However, this assumption is not accurate as in the presence of obstacles, the volume accessible to the ellipsoidal particles to diffuse will depend on the width of the channel formed between the obstacles. Thus, the diffusivity of the ellipsoids $D_T(x)$ will be position dependent.

Reguera and Rubí⁶⁵ considered the short time diffusion of the point particles to be position dependent such that $D_T(x) = D_2^P/[1 + w'(x)/4]^{1/3}$. The effective diffusivity D_T^{RR} is given by

$$\frac{D_T^{RR}}{D_2^P} = \frac{1}{(1 - \frac{\pi}{4} f_w^2)} \times \frac{1}{\left[f_w \int_0^{\pi/2} \frac{(\cos \phi)^{1/3} d\phi}{(1 - f_w \cos \phi)} + 1 - f_w \right]}, \quad (27)$$

where f_w is given as $(\sqrt{1/\rho_o} - w)/(\sqrt{1/\rho_o} - d_p)$ with $\sqrt{1/\rho_o}$ being the lattice constant for the obstacle configuration and d_p being the length of the minor axis. At $f_w = 0$, we have infinitely thin cylinders and the channel opening w between the cylinders reaches its maximum value, which is equal to the lattice constant $\sqrt{1/\rho_o}$. At $f_w = 1$, the channel width is so small that ($w = d_p$) no ellipsoidal particle can escape; thus, the diffusivity perpendicular to the cylindrical axis goes to zero. To compare the diffusivity of a particle with a finite volume with that of the point particle model, we have kept q the trap size constant while changing f_w . In other words, both the lattice constant and the radius of the obstacles are varied to maintain the desired trap size q and channel width w , which are the relevant parameters governing the diffusivity of the ellipsoidal particles.

We calculated the long-time diffusivity of the spheroids in the plane perpendicular to the axis of the cylinder by changing f_w at different constant q values as shown in Fig. 8. The resulting two-dimensional translational diffusivity D_T^2 for the single particle at different f_w is normalized by D_2^P , which is also 2d diffusivity at $f_w = 0$ for a particular trap size q . D_T^2 for spheres [Fig. 8(a)] agrees with D_T^{RR} (green solid line); however, D_T^{FJ} overestimates the diffusivity of the ellipsoidal particles. When we increase the anisotropy of the ellipsoidal particle by changing p , we observe significant deviation from the analytical calculation; see Figs. 8(b)–8(d). For the prolate particles, the deviation from the analytical calculation happens when $f_w > 0.5$ as can be observed in Figs. 8(b) and 8(c). It can also be observed that when the trap size q is smaller, the deviation from analytical calculation happens at lower f_w . For the disk like particles [Fig. 8(d)], the deviation from the analytic calculation happens at a smaller f_w than for the needle like particles. Also note that in the absence of obstacles, both the system $p = 0.333$ and 3.0 show almost the same diffusivity.³⁹

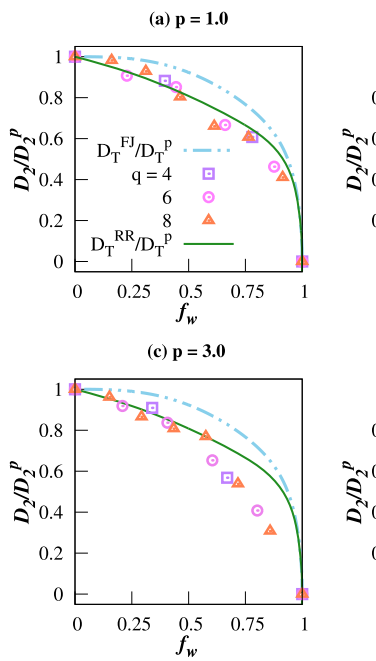


FIG. 8. Variation in 2D translational diffusivity D_2/D_2^p of a single spheroid shown at different cage openings f_w , measured in the laboratory frame in the plane perpendicular to the cylindrical axis, for $w = 4$ (square), 6 (circle), and 8 (triangle). (a) For spheroids with $p = 1.0$, (b) 2.0, (c) 3.0 (rod like particles), and (d) 0.333 (disk like particles). All the diffusivities have been normalized by D_2^p , the diffusivity at $f_w = 0$ (for the constant radius of obstacles $\rho_o = 0$).

To compare with the expression of the diffusivity given for the point particles, we calculated D_2 and normalized with D_2^p , which is the maximum D_2 possible at a constant q (at $f_w = 0$) for a given finite volume fraction $\phi = 0.2$. For the spherical particles, the diffusivity follows the analytical curve as in the case of single particle diffusivity as shown in Fig. 9(a). However, for the ellipsoidal particles also, we have less deviation from the analytical curve in comparison with the single particle diffusivity, as shown in Figs. 9(b)–9(d) calculated for $p = 2.0$, 3.0, and 0.333, respectively. It indicates that for the particles at a finite volume fraction in the isotropic phase, the caging effect due to the obstacles remains the same regardless of the shape of the particle.

For a particular constant q value, the diffusivity will be maximum D_2^p at $f_w = 0.0$ (at constant $r_o = 0$). Figure 10 shows variation in D_2^p with q , where the x-axis is scaled as $1/1 + q$, which varies between 0 and 1, as q varies between ∞ and 0. $q = \infty$ represents a system without obstacles. In the larger trap size regions, the diffusivity varies almost linearly regardless of their shapes [Figs. 10(a) and 10(b)]. One difference between the Lorentz gas model and the finite size particle is that D_2^p of the Lorentz gas model would be maximum and same at all the q values⁶⁴ for $f_w = 0$. To find out the variation in D_2^p in the small trap size regions (comparable with the particle's size), we calculated diffusivity at $r_o = 2.0$ [Fig. 10(c)] shows D_2^p at a finite concentration and Fig. 10(d) for single particles]. For the spherical particles (square points), diffusivity drops abruptly. However, the drop in the diffusivity of the anisotropic particles remains linear almost throughout the whole q regions.

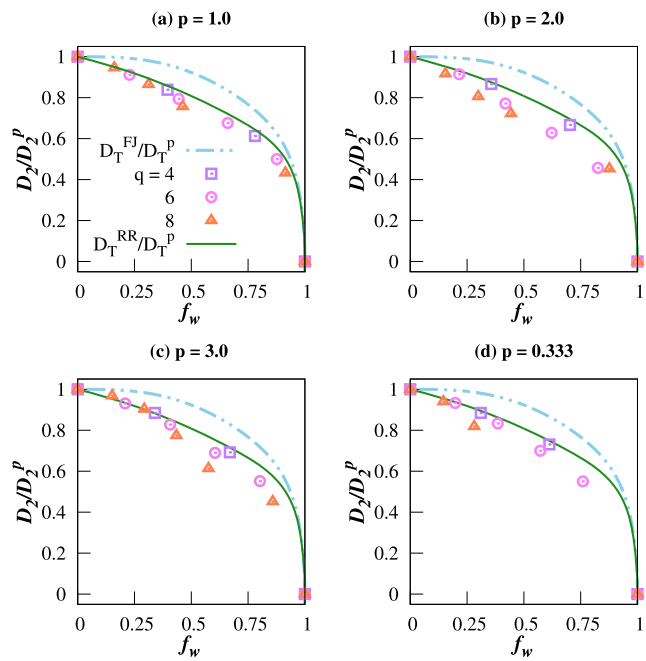


FIG. 9. Variation in 2D translational diffusivity D_2/D_2^p of spheroids at a finite concentration ($\phi = 0.2$), shown at different cage openings f_w , for $w = 4$ (square), 6 (circle), and 8 (triangle). (a) For spheroids with $p = 1.0$, (b) 2.0, (c) 3.0, and (d) 0.333.

The dynamics of the ellipsoidal particle is related to the volume accessible to the center of mass of the ellipsoidal particles also known as accessible volume, due to the finite size of the obstacles and the ellipsoids. If the accessible volume is small, it will lead to caging and dimensional confinement. The diffusivity of the ellipsoidal particles goes to zero when the channel width is close to the ellipsoidal particle's size. The accessible volume is related to the chemical potential of the hard sphere particle system⁶⁶ given by $\mu/k_B T = -\ln \frac{\phi_a}{\phi}$, where μ is the chemical potential of the hard sphere particles at volume fraction ϕ and having an accessible volume ϕ_a . In Fig. 11, we have plotted the chemical potential calculated using Widom's particle insertion method for different ϕ with varying w/d_o and q/d_o at different ϕ_o . For constant w/d_o values, $\mu/k_B T$ decreases with an increase in q/d_o and becomes constant in the large q/d_o regime corresponding to a large accessible volume. When $w < d_o$ and $q < d_o$, $\mu/k_B T$ increases and it becomes increasingly difficult to access the free volume for the ellipsoidal particle. A higher $\mu/k_B T$ represents a lower accessible volume, which leads to a decrease in the diffusivity of the particles.

Experimentally, the diffusivity of the tracer particles has been shown to fall exponentially with the increase in the concentration of heavy globular proteins in the aqueous solution,² due to the decrease in the accessible volume for the tracer particle. To show the effect of the confinement and excluded volume, ϕ and ϕ_a , on the translational diffusivity, we have shown D_T/D_T^p as a function of Widom's chemical potential $\mu/k_B T$ for the spherical [Fig. 12(a)] and spheroidal particles [prolate, $p = 2.0$ Fig. 12(b)]. At this p , we will

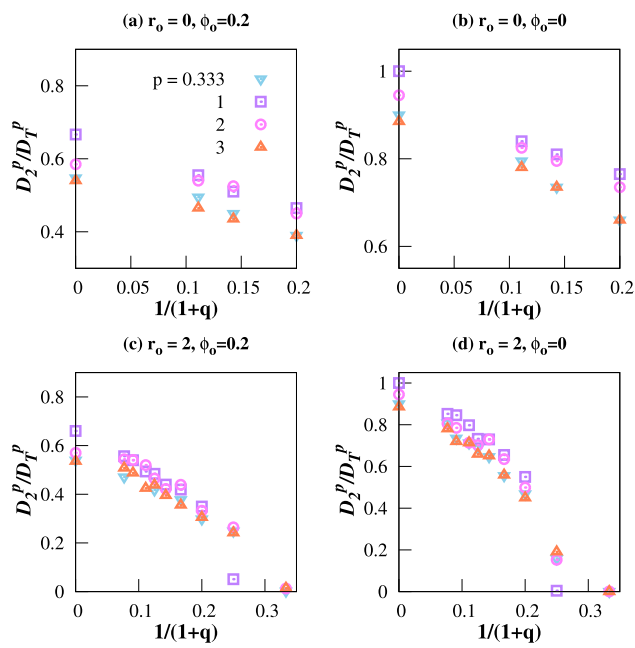


FIG. 10. Variation in D_2^p/D_T^p with $1/(1+q)$, where D_2^p is the diffusivity shown for the cylinders with a constant and infinitely thin radius ($\rho_o = 0$). (a) At finite particle's concentration and (b) at infinitely dilute concentration. Variation in D_2^p also shown for the finite radius ($\rho_o = 2$) (c) at finite particle's concentration and (d) at infinitely dilute concentration, where all the diffusivity values have been scaled by D_T^p , the diffusivity of single spheroids in the bulk phase.

always have an isotropic fluid phase irrespective of ϕ . The diffusivity of the system with respect to $\mu/k_B T$ is shown at a finite spheroid concentration and infinite spheroid dilution (single particle) in comparison with the diffusivity of hard spheroids at different ϕ without the presence of obstacles. We can observe that a sudden sharp fall in the diffusivity of the spherical particle and prolate particle as w/d_o falls below 1.0 (size of the particle) as shown in Figs. 12(a) and 12(b), respectively. Interestingly, in the case of single particle,

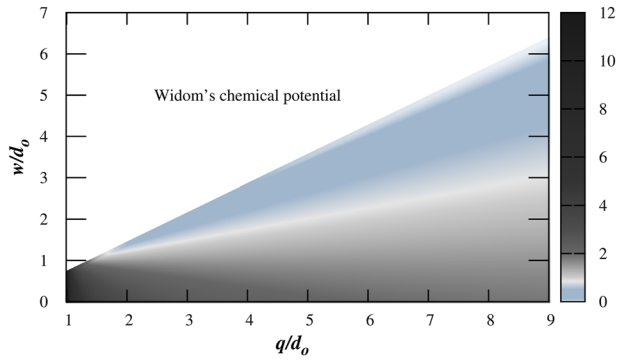


FIG. 11. Widom's chemical potential is shown by the colored map in the $q-w$ plane.

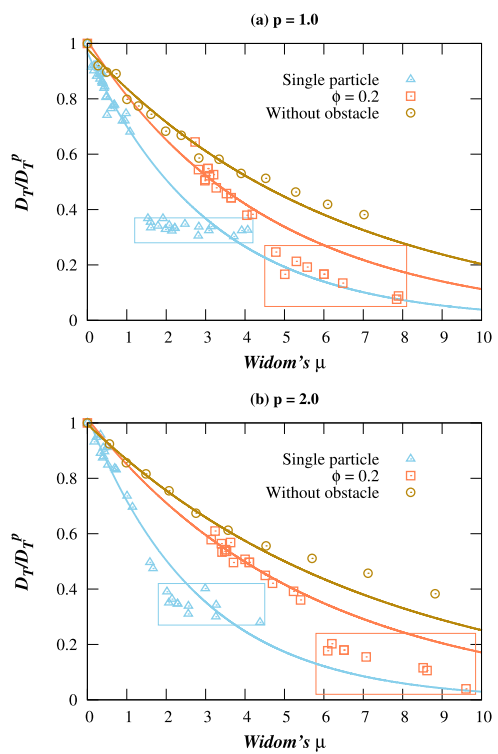


FIG. 12. Translational diffusivity D_T/D_T^p normalized by the diffusivity of the particle in infinite dilution D_T^p is shown as a function of Widom's chemical potential for (a) spherical particles and (b) prolate particles. The blue triangles represent the single particle diffusivity within the presence of obstacles. The coral squares represent the diffusivity at a finite particle concentration with $\phi = 0.2$, compared with the diffusivity at different particle concentrations ϕ in the absence of obstacles represented by dark-golden circles. The solid lines represent the exponential fits. The points inside the rectangular bracket represent the system with $2d$ confinement ($s < 1.0$), where the particles can only move in the $1d$ pour confined by the cylindrical obstacles.

the diffusion coefficient becomes independent of the obstacle concentration for both spherical and prolate particles. The reason is that the sphere and the prolate particle can only diffuse along one dimension, which is parallel to the axis of the cylinder. The diffusion coefficient D_T/D_T^p for a spherical and the prolate particle along one dimension in simulations is ~ 0.35 , which is the approximate value we observe for spheres. At a finite concentration ($\phi = 0.2$), the diffusivity keeps decreasing with increasing $\mu/k_B T$ due to the increase in ϕ , as the effective accessible volume fraction decreases due to the excluded volume between the two ellipsoidal particles. Also with the increase in the radius of the cylindrical obstacle, all the ellipsoidal particles may get aligned in a column.³ This is the minimum energy configuration for a single prolate particle in the presence of the cylindrical obstacle. Thus, for a finite volume fraction, once the ellipsoids are aligned, then the diffusion is only possible along one dimension, which is along the direction of the cylindrical axis. We observe that the diffusivity of the ellipsoidal particle at $\phi = 0.2$ [Figs. 12(a) and 12(b)] follows the fitted exponential curve, which falls suddenly to a lower value. This is again due to the one-dimensional confinement

of the ellipsoidal particle. Compared to the single particle diffusion, which was a constant after confinement along one dimension for $\phi = 0.2$ even after confinement, the diffusion coefficient falls due to the finite volume fraction of the ellipsoids. In all the cases, the diffusivity in the presence of obstacles remains lower than the diffusivity in the spherical particle at finite ϕ without the obstacle.

To show the effect on the dynamics of highly anisotropic particles, we took oblate and prolate particles with $p = 3.0$ and $p = 0.333$, respectively. It should be noted that the presence of cylindrical obstacles does not change the isotropic–nematic boundary in the ϕ - p plane. Figures 13(a) and 13(b) show the variation in D_T/D_T^P of both prolate and oblate particles, respectively, as a function of μ , calculated at $\phi = 0.2$. At this ϕ , the systems corresponding to both prolate and oblate remain isotropic for all the points shown in Figs. 13(a) and 13(b). The translational diffusivity behaves in the same way as a spherical particle system. The ellipsoidal system still shows a sudden drop with μ as the diffusivity perpendicular to the cylinder axis drops to zero as discussed earlier for the spherical system.

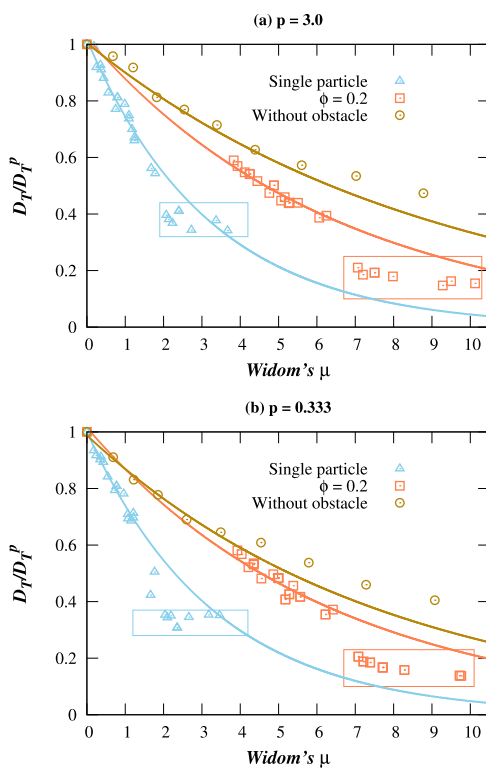


FIG. 13. Translational diffusivity D_T/D_T^P normalized by the diffusivity of the particles in infinite dilution D_T^P is shown as a function of Widom's chemical potential for highly anisotropic particles: (a) prolate ($p = 3.0$) and (b) oblate ($p = 0.333$). The blue triangles represent the single particle diffusivity within the presence of obstacles. The coral squares represent the diffusivity at a finite particle concentration with $\phi = 0.2$, compared with the diffusivity at different particle concentrations ϕ in the absence of obstacles represented by dark-golden circles. The solid lines represent the exponential fits. The points inside the rectangular bracket represent the system with $2d$ confinement ($\mu < 1.0$), where the particles can only move in the $1d$ pour confined by the cylindrical obstacles.

Unlike the translational diffusivity, which depends dominantly on the channel width w/d_o , the rotational diffusivity is found to depend dominantly on the trap size q/d_o . At a large q/d_o , the rotational diffusivity remains decoupled with the translational diffusivity in the isotropic phase. Figure 14(a) shows the variation in rotational diffusivity D_R/D_R^P with q/d_o . D_R/D_R^P is shown to stagnate quickly with the increase in q/d_o reaching the diffusion coefficient of the bulk system in the absence of obstacles ($D_R^P \sim 0.33, 0.56, 0.66$, for $p = 3.0, 0.33, 2.0$, respectively, calculated at $\phi = 0.2$) for both prolate and oblate systems. However, in the nematic phase, the disk like particles show strong coupling between translational and rotational diffusivities. In the absence of obstacles, the rotational motion in the nematic phase shows a sub-diffusive behavior in the long time limit. However, in the presence of obstacles with high $r_o/d > 4$, D_R/D_R^P of the oblate particles present in the nematic phase near the obstacle's comes out of the dynamic arrest configuration. As it has been shown in the $g(\theta)$ calculation [Fig. 6(a)], with a higher radius, the obstacle structure gets frustrated locally, providing space for the flipping of the particle. The region over which we observe the anomalous behavior is shown as the shaded region in Fig. 14(b) in the $q/d - r_o/d$ plane, where the disk like particles with $p = 0.25$ were considered.

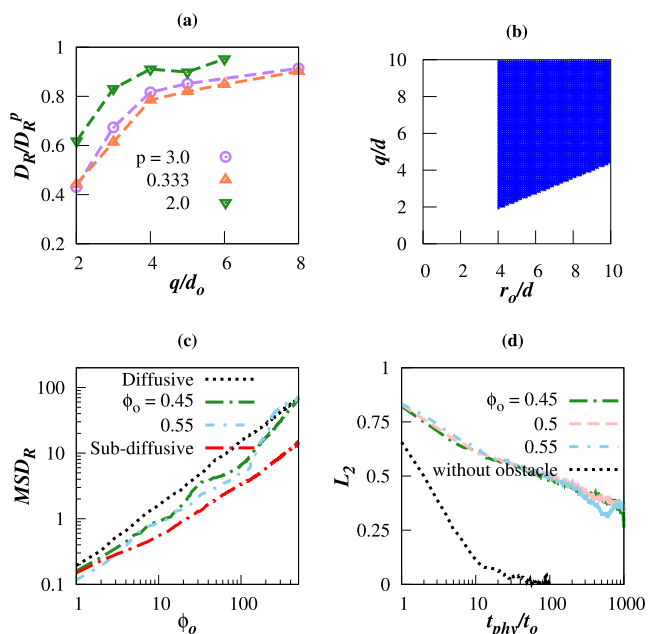


FIG. 14. (a) Rotational diffusivity D_R/D_R^P is shown with the change in obstacle configuration, for $p = 3.0$ (circles), $p = 0.333$ (upper triangle), and $p = 2.0$ (lower triangle), at particle concentration $\phi = 0.2$. (b) Blue region shown in the $q - r_o$ plane represents the configuration of obstacles, where the disk like particles show a diffusive behavior at long time scale despite being in nematic phase (for $\phi_o > 0.425$). (c) MSD_R is shown for the oblate particles ($p = 0.25$) flipping at ($\phi = 0.45$), for different obstacle concentrations ϕ_o , for a large obstacle size $r_o = 5.0$. The red line shows MSD_R averaged over all the particles. The black line is a guide to the perfectly diffusive behavior. (d) Decay of L_2 with time is shown. Long dashed lines represent the different ϕ_o as given in the legend, compared with the decay of L_2 for $D_R/D_R^P = 0.2$ in the absence of obstacles calculated at $\phi = 0.45$ (black short dashed line).

The oblate particle close to the obstacles flips along the major axis, contributing to the higher value of diffusivity. We observe the dynamics deviating away from being sub-diffusive and entering the super-diffusive phase. The rotational mean-square-displacement (MSD_R)⁶⁷ is shown in Fig. 14(c), where we observe a shift from the short time super-diffusive to long time sub-diffusive regime. As for MSD_R , only the rotating particle contributes because all the other particles are in the nematic phase and hence show a sub-diffusive behavior [see Fig. 14(c), red dashed line]. To show that this is a local effect, we have calculated the orientational self-correlation L_2 as follows:

$$L_2(t) = \frac{1}{N} \sum_i \frac{1}{2} (3\hat{n}_i(\tau+t) \cdot \hat{n}_i(\tau) - 1), \quad (28)$$

where $n_i(t)$ is the orientation of the i th particle at time t . We have shown the decay of L_2 as a black dashed line in Fig. 14(d) for a system without obstacle, with nearly the same $D_R/D_R^p = 0.19$ (at $\phi = 0.4$). L_2 decays to 0 at $t_{phy} > 20.0$. In the presence of obstacles where the bulk is found to be in the nematic phase and shows $D_R/D_R^p > 0.19$, L_2 can be observed not decaying [colored dashed lines in Fig. 14(d)]. Thus, globally, the system is in nematic phase, which leads to a decline in the rotational dynamics. However, in the presence of obstacles, the particles are flipping locally and contributing to the super-diffusive behavior. In this way, the system maintains the nematicity despite few of the particles being out of the arrested rotational dynamics phase. The reason for the flipping of oblate particles may be the misalignment of the particles caused by the presence of obstacles [Fig. 6(a)]. However, in the prolate case, the particle's alignment enhances and remains parallel to the cylindrical axis [Fig. 6(b)]. Therefore, the rotational dynamics of the prolate particles in the presence of obstacles remains frozen.

IV. CONCLUSION

Experimentally, numerous studies have been performed by confining the particles in various geometries. In almost all these studies, it has been shown that the shape anisotropy of the particles enhances the motion of the self-propelled particle. However, in the passive particle system, dynamics is governed by the structure of the fluid. The theoretical prediction of diffusivity for the point particles is modified to incorporate a finite volume particle, which agrees with our simulation results. However, with the increase in shape anisotropy, the diffusivity deviates from the proposed theoretical prediction. At a finite volume fraction, the dynamics of the system become dependent upon structural properties. The structural property of the spheroidal particle as a result of the introduction of obstacles in the system influences the dynamics. As shown in the case of oblate particles, the rotational diffusivity couples with translational diffusivity, resulting in the flipping motion, leading to a super-diffusivity behavior. In the present study, for a low particle concentration regime, the translational diffusivity of the anisotropic particles behaves nearly the same way as the system of spherical particles. For a single particle as well as for finite ϕ , diffusing in the cylindrical pores with extreme confinement, the long-time translational diffusivity behaves like a one-dimensional system, where diffusivity scales to one by a third of the diffusivity of the bulk system.

In the presence of obstacles, the nematic phase has been observed to show exciting results. We have shown the nematic director being controlled by the presence of cylindrical obstacles. The kinetics of the evolution of the particles' alignment showed that the spheroidal particles preferred to align quickly along the axis of the cylindrical obstacles. We hope that the present study would help us design a system where the nematic alignment can be controlled by the surface effects of the obstacles.

ACKNOWLEDGMENTS

V.A.V. acknowledges CSIR-UGC and the institute for funding this research.

AUTHOR DECLARATIONS

Conflict of Interest

The authors have no conflicts to disclose.

Author Contributions

Vikki Anand Varma: Conceptualization (equal); Data curation (lead); Formal analysis (equal); Funding acquisition (lead); Investigation (equal); Methodology (equal); Project administration (supporting); Resources (supporting); Supervision (supporting); Validation (equal); Visualization (equal); Writing – original draft (equal); Writing – review & editing (equal). **Sujin B. Babu:** Conceptualization (lead); Data curation (supporting); Formal analysis (lead); Funding acquisition (supporting); Investigation (lead); Methodology (lead); Project administration (lead); Resources (lead); Supervision (lead); Validation (lead); Writing – original draft (equal); Writing – review & editing (equal).

DATA AVAILABILITY

The data that support the findings of this study are available from the corresponding author upon reasonable request.

REFERENCES

- ¹D. Gomez and S. Klumpp, *Phys. Chem. Chem. Phys.* **18**, 11184 (2016).
- ²D. S. Banks and C. Fradin, *Biophys. J.* **89**, 2960 (2005).
- ³M. Zarif and R. K. Bowles, *Phys. Rev. E* **101**, 012908 (2020).
- ⁴T. S. Domingues, R. R. Coifman, and A. Haji-Akbari, *J. Phys. Chem. B* **127**, 5273 (2023).
- ⁵T. Motegi, H. Nabika, and K. Murakoshi, *Phys. Chem. Chem. Phys.* **15**, 12895 (2013).
- ⁶T. Sentjabrskaja, E. Zaccarelli, C. De Michele, F. Sciortino, P. Tartaglia, T. Voigtmann, S. U. Egelhaaf, and M. Laurati, *Nat. Commun.* **7**, 11133 (2016).
- ⁷H. W. Cho, G. Kwon, B. J. Sung, and A. Yethiraj, *Phys. Rev. Lett.* **109**, 155901 (2012).
- ⁸S. Lifson and J. L. Jackson, *J. Chem. Phys.* **36**, 2410 (1962).
- ⁹M. Jardat, B. Hribar-Lee, and V. Vlachy, *Phys. Chem. Chem. Phys.* **10**, 449 (2008).
- ¹⁰P. Illien, O. Bénichou, G. Oshanin, A. Sarracino, and R. Voituriez, *Phys. Rev. Lett.* **120**, 200606 (2018).
- ¹¹H. Khalilian and H. Fazli, *J. Chem. Phys.* **145**, 164909 (2016).

- ¹²D. M. van Roon, G. Volpe, M. M. Telo da Gama, and N. A. M. Araújo, *Soft Matter* **18**, 6899 (2022).
- ¹³R. Zwanzig, *J. Phys. Chem.* **96**, 3926 (1992).
- ¹⁴J. M. Rubí, *Europhys. Lett.* **127**, 10001 (2019).
- ¹⁵A. Berezhkovskii and A. Szabo, *J. Chem. Phys.* **135**, 074108 (2011).
- ¹⁶T. Bertrand, Y. Zhao, O. Bénichou, J. Tailleur, and R. Voituriez, *Phys. Rev. Lett.* **120**, 198103 (2018).
- ¹⁷T. Guérin and D. S. Dean, *Phys. Rev. Lett.* **115**, 020601 (2015).
- ¹⁸A. Filippov, H. Soenen, J. Blom, and O. N. Antzutkin, *ACS Omega* **8**, 36534 (2023).
- ¹⁹J. Kurzidim, D. Coslovich, and G. Kahl, *Phys. Rev. E* **82**, 041505 (2010).
- ²⁰H. Berry and H. Chaté, *Phys. Rev. E* **89**, 022708 (2014).
- ²¹M.-B. Luo and D.-Y. Hua, *ACS Omega* **8**, 34188 (2023).
- ²²J. M. Sancho, A. M. Lacasta, K. Lindenberg, I. M. Sokolov, and A. H. Romero, *Phys. Rev. Lett.* **92**, 250601 (2004).
- ²³H. Hijar, *Phys. Rev. E* **102**, 062705 (2020).
- ²⁴Y. Gu and N. L. Abbott, *Phys. Rev. Lett.* **85**, 4719 (2000).
- ²⁵F. Nakai, M. Kröger, T. Ishida, T. Uneyama, Y. Doi, and Y. Masubuchi, *Phys. Rev. E* **107**, 044604 (2023).
- ²⁶F. van Swol, L. J. Douglas Frink, A. P. Malanoski, and D. N. Petsev, *J. Chem. Phys.* **159**, 084705 (2023).
- ²⁷H.-L. Yeh and J. J. Juárez, *Exp. Therm. Fluid Sci.* **121**, 110282 (2021).
- ²⁸W. P. Krekelberg, V. K. Shen, J. R. Errington, and T. M. Truskett, *J. Chem. Phys.* **135**, 154502 (2011).
- ²⁹F. Zhou, H. Wang, and Z. Zhang, *Langmuir* **36**, 11866 (2020).
- ³⁰M. Brun-Cosme-Bruny, E. Bertin, B. Coasne, P. Peyla, and S. Rafaï, *J. Chem. Phys.* **150**, 104901 (2019).
- ³¹T. Guérin, N. Levernier, O. Bénichou, and R. Voituriez, *Nature* **534**, 356 (2016).
- ³²L. Dai, D. R. Tree, J. R. C. van der Maarel, K. D. Dorfman, and P. S. Doyle, *Phys. Rev. Lett.* **110**, 168105 (2013).
- ³³M. J. Simpson and M. J. Plank, *Results Phys.* **7**, 3346 (2017).
- ³⁴Y. Farah, D. Loghin, A. Tzella, and J. Vanneste, *Proc. R. Soc. A* **476**, 20200072 (2020).
- ³⁵M. Mangeat, T. Guérin, and D. S. Dean, *J. Chem. Phys.* **152**, 234109 (2020).
- ³⁶A. J. Ellery, R. E. Baker, and M. J. Simpson, *Phys. Biol.* **12**, 066010 (2015).
- ³⁷L. Dagdug, M.-V. Vazquez, A. M. Berezhkovskii, V. Y. Zitserman, and S. M. Bezrukov, *J. Chem. Phys.* **136**, 204106 (2012).
- ³⁸S. K. Ghosh, A. G. Cherstvy, and R. Metzler, *Phys. Chem. Chem. Phys.* **17**, 1847 (2015).
- ³⁹V. A. Varma, I. Malhotra, and S. B. Babu, *Phys. Rev. E* **106**, 014602 (2022).
- ⁴⁰A. Poniewierski and R. Holyst, *Phys. Rev. A* **38**, 3721 (1988).
- ⁴¹T. Khatun, M. D. Choudhury, T. Dutta, and S. Tarafdar, *Phys. Rev. E* **86**, 016114 (2012).
- ⁴²T. Boeck, H.-A. Bahr, S. Lampenscherf, and U. Bahr, *Phys. Rev. E* **59**, 1408 (1999).
- ⁴³B. Langeslay, W. Fahy, and G. Juarez, *arXiv:2401.17222* (2024).
- ⁴⁴M. Robert de Saint Vincent, M. Abkarian, and H. Tabuteau, *Soft Matter* **12**, 1041 (2016).
- ⁴⁵Z. Shireen and S. B. Babu, *J. Chem. Phys.* **147**, 054904 (2017).
- ⁴⁶Z. Shireen and S. B. Babu, *Soft Matter* **14**, 9271 (2018).
- ⁴⁷M. Adams, Z. Dogic, S. L. Keller, and S. Fraden, *Nature* **393**, 349 (1998).
- ⁴⁸S. Varga, A. Galindo, and G. Jackson, *J. Chem. Phys.* **117**, 7207 (2002).
- ⁴⁹B. Senyuk, C. Meng, and I. I. Smalyukh, *Langmuir* **38**, 9099 (2022).
- ⁵⁰J. W. Perram, J. Rasmussen, E. Praestgaard, and J. L. Lebowitz, *Phys. Rev. E* **54**, 6565 (1996).
- ⁵¹S. Babu, J. C. Gimel, and T. Nicolai, *J. Chem. Phys.* **125**, 184512 (2006).
- ⁵²Z. Shireen, T. Curk, C. Brandl, and S. B. Babu, *ACS Omega* **8**, 37225 (2023).
- ⁵³I. Malhotra and S. B. Babu, *J. Chem. Phys.* **151**, 084901 (2019).
- ⁵⁴M. Yadav, V. A. Varma, and S. B. Babu, *J. Mol. Liq.* **399**, 124404 (2024).
- ⁵⁵V. A. Varma, Kritika, J. Singh, and S. B. Babu, "Self assembly of patchy anisotropic particle forming free standing monolayer film," *Adv. Theory Simul.* **6**(3), 2200666 (2023).
- ⁵⁶V. A. Varma, S. Jaglan, M. Y. Khan, and S. B. Babu, *Phys. Chem. Chem. Phys.* **26**, 1385 (2024).
- ⁵⁷A. Poniewierski, R. Holyst, *Phys. Rev. A* **38**, 3721 (1988).
- ⁵⁸D. Medlin and G. Snyder, *Curr. Opin. Colloid Interface Sci.* **14**, 226 (2009).
- ⁵⁹K. H. Kil, A. Yethiraj, and J. S. Kim, *Phys. Rev. E* **101**, 032705 (2020).
- ⁶⁰S. Babu, J.-C. Gimel, T. Nicolai, and C. De Michele, *J. Chem. Phys.* **128**, 204504 (2008).
- ⁶¹C. De Michele, R. Schilling, and F. Sciortino, *Phys. Rev. Lett.* **98**, 265702 (2007).
- ⁶²G. Goel, W. P. Krekelberg, M. J. Pond, J. Mittal, V. K. Shen, J. R. Errington, and T. M. Truskett, *J. Stat. Mech.: Theory Exp.* **2009**, P04006.
- ⁶³I. C. Kim and S. Torquato, *J. Chem. Phys.* **96**, 1498 (1992).
- ⁶⁴J. Machta and R. Zwanzig, *Phys. Rev. Lett.* **50**, 1959 (1983).
- ⁶⁵D. Reguera and J. M. Rubí, *Phys. Rev. E* **64**, 061106 (2001).
- ⁶⁶S. Babu, J. C. Gimel, and T. Nicolai, *J. Phys. Chem. B* **112**, 743 (2008).
- ⁶⁷K. V. Edmond, M. T. Elsesser, G. L. Hunter, D. J. Pine, and E. R. Weeks, *Proc. Natl. Acad. Sci. U. S. A.* **109**, 17891 (2012).